Research Square

Preprints are preliminary reports that have not undergone peer review.
They should not be considered conclusive, used to inform clinical practice,
or referenced by the media as validated information.

Thermally controllable diffractive processor using hybrid metasurfaces

Xiaofei Zang

xfzang@usst.edu.cn

University of Shanghai for Science and Technology https://orcid.org/0000-0001-8557-895X

Guannan Wang

University of Shanghai for Science and Technology

Xinyu Huang

Nanjing University

Teng Zhang

University of Shanghai for Science and Technology

Zhiyu Tan

University of Shanghai for Science and Technology https://orcid.org/0000-0002-4117-2525

Jingbo Wu

Nanjing University https://orcid.org/0000-0003-2969-5670

Biaobing Jin

Nanjing University https://orcid.org/0000-0001-9506-8355

Yiming Zhu

University of Shanghai for Science and Technology https://orcid.org/0000-0003-2353-5713

Songlin Zhuang

University of Shanghai for Science and Technology

Article

Keywords:

Posted Date: March 10th, 2026

DOI: https://doi.org/10.21203/rs.3.rs-8811837/v1

License: This work is licensed under a Creative Commons Attribution 4.0 International License.
Read Full License

Additional Declarations: There is no conflict of interest

Thermally controllable diffractive processor using hybrid metasurfaces

Guannan Wang[1,#], Xiaofei Zang[1,3*, #], Xinyu Huang[2,#], Teng Zhang[1], Zhiyu Tan[1], Zhe Gao[1], Jinggui Sun[1], Jingbo Wu[2*], Biaobing Jin[2], Yiming Zhu[1,3*], Songlin Zhuang[1]

Correspondence: Xiaofei Zang (xfzang@usst.edu.cn) or Jingbo Wu (jbwu@nju.edu.cn) or Yiming Zhu (ymzhu@usst.edu.cn)

[1]Terahertz Technology Innovation Research Institute, and Shanghai Key Lab of Modern Optical System, University of Shanghai for Science and Technology, No. 516 JunGong Road, Shanghai 200093, China
[2]Research Institute of Superconductor Electronics & Key Laboratory of Optoelectronic Devices and Systems with Extreme Performances of MOE, School of Electronic Science and Engineering, Nanjing University, Nanjing 210023, China
[3]Shanghai Institute of Intelligent Science and Technology, Tongji University, Shanghai 200092, China

[#]These authors contributed equally: Guannan Wang, Xiaofei Zang, Xinyu Huang

Abstract

All-optical diffractive neural networks (DNNs) have garnered notable attention in artificial intelligence because of their unprecedented ability to perform complex tasks at the speed of light. However, current DNNs designs mainly rely on non-tunable diffractive components with fixed functionality. Here, to introduce active diffraction units into DNNs at terahertz (THz) spectrum, we report a hybrid metasurface-based thermally controllable diffractive processor that mimics task-switchable DNNs using thermally reconfigurable meta-neurons composed of vanadium dioxide (VO_2) resonators and gold resonators. The optical response of the network layer of this processer can be dynamically switched based on ambient temperature to meet dynamic task requirements. We experimentally validate the efficacy of the processer through classification tasks involving single and double handwritten digits as well as fashion products. Moreover, we propose an information encryption framework that leverages ambient temperatures as decryption keys. This temperature-dependent all-optical processor with multiplexing capability paves the way for the next-generation high-speed optical computing, dynamic optical systems, and secure communications.

Introduction

In the rapidly evolving era of information, artificial intelligence (AI) is revolutionizing industries spanning from image recognition[1-3] to human-like natural language processing[4,5]. The success of AI has pushed an unprecedented demand for the computing systems with high-speed and high-parallelism with low power consumption[6]. However, traditional electronic neural networks are increasingly approaching their physical limit due to the constraint of Moore's law and Dennard scaling[7]. Optical neural networks (ONNs), which process matrix operations through light propagation, have been extensively explored for decades to address these computational bottlenecks[8]. For instance, ONNs have been successfully applied in convolution neural network[9,10], Mach-Zehnder interferometer networks[11,12], spoof plasmonic neural network[13], and fully forward mode learning[14].

With the progressive advancement in ONNs, all-optical diffractive neural networks (DNNs) that are constructed by cascaded diffractive surfaces to process the predesigned tasks (based on complex computing and inference) have emerged as a landmark paradigm in this filed[15,16]. This free-space all-optical processing method exhibits notable advantages in parallel image processing and large-scale computing, including pattern recognition[17-19], imaging[20-22], information encryption[23-25], and AI-generated[26]. However, current research on DNNs primarily focuses on fixed-functionality diffractive layers with passive diffractive units, which limit their adaptability to dynamic task requirements. While promising studies have reported programmable diffractive neural networks, these designs suffer from large volumes due to their operation in the microwave range[27,28]. Notably, miniaturization and integration are important design objectives in most DNN architectures[29-31]. Therefore, developing a compact and dynamic diffraction processing platform to overcome this dilemma represents a significant and pressing challenge.

In this work, we introduce a thermally controllable diffractive processor (TDP) constructed with thermally reconfigurable meta-neurons, operating in the terahertz (THz) region. The proposed devices enable dynamic diffraction computing on a compact and efficient platform. Leveraging the unparalleled light-manipulation capability of metasurfaces[32-38] we design the TDP using a hybrid metasurface, which integrates thermally reconfigurable gold-VO_2 hybrid resonators with static gold resonators to form the meta-neurons. The unique

architecture of the TDP allows its optical response and functionality to dynamically switch according to ambient temperature to perform diverse computational tasks. In experiment, we construct the TDP as a dynamic object classification processor, which can realize temperature-dependent classification task switching functionality. First, we demonstrate its capability to classify single objects, validating the efficacy of the TDP. At two pre-designed ambient temperatures, this processor can classify handwritten digits and fashion products, respectively. Then, a TDP capable of classifying double objects is fabricated and demonstrated, which can switch between classifying double handwritten digits and double fashion products at two different ambient temperatures. In addition, we propose a potential application of this processing platform in secure information transmission by using ambient temperature as decryption keys. The TDP offers a thermally controlled solution for THz-band DNNs, unlocking new possibilities for dynamic all-optical computing.

Results

TDP concept design

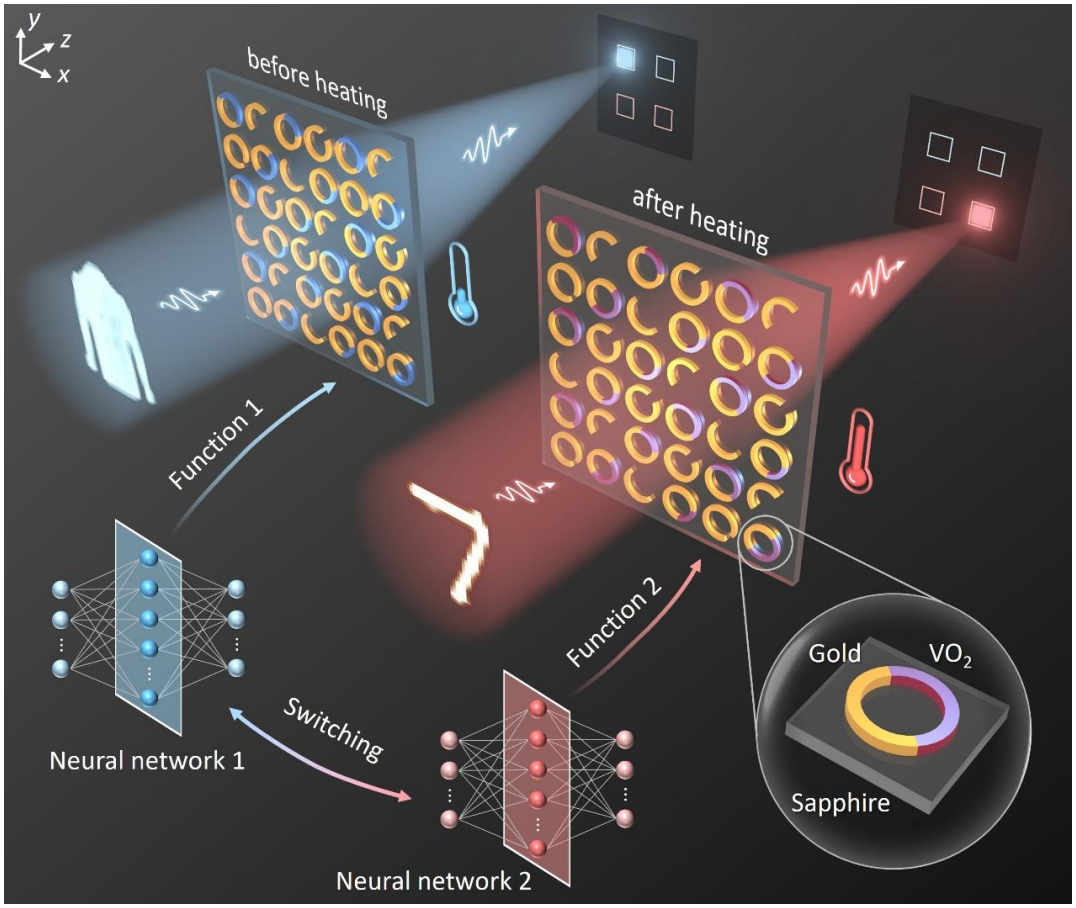


Fig.1 Schematic of the TDP. At two distinct ambient temperatures, the TDP achieves functional switching between Neural network 1 and Neural network 2 through insulator-metal transition. Under the illumination of *x*-polarized THz waves propagating along the *z*-axis, it classifies inputs from Fashion-MNIST and MNIST datasets, respectively, showcasing its temperature-dependent reconfigurable capability.

Figure 1 shows the schematic of the TDP operating at two different ambient temperatures. The TDP is constructed by arrays of meta-neurons, including complementary ring structure of VO_2 and gold resonator (C-structure), as well as gold-only resonator structures (G-structure) on a sapphire substrate. When operating at room temperature about 300 K (indicated by the blue thermometer on the left), the VO_2 resonators within the meta-neurons exhibits its insulating state (represented by blue). Under the illumination of *x*-polarized THz waves propagating along the z-axis, the TDP functions as the first neural network (marked as Neural network 1). An input of a coat from the Fashion-MNIST dataset is generated by a gold mask (fabricated masks are shown in Supplementary Section 1) and then projected and processed by the TDP. Subsequently, the *y*-polarized THz waves that carry the recognition results of the coat are accurately diffracted to the upper left corner of the output plane, performing the classification task for Fashion-MNIST dataset. After heating to a temperature of 341 K, the TDP operates at an elevated temperature, and the VO_2 resonators within the meta-neurons transform into its metallic state, generating a different optical response. Meanwhile, the TDP switches its characteristics to a second neural network (marked as Neural network 2) with distinct functionality under the illumination of *x*-polarized THz waves to perform another task. The output *y*-polarized THz waves, diffracted to the bottom right corner, represent the classification result of an input handwritten digit 7 from MNIST dataset, showcasing the temperature-dependent reconfigurable capability of the TDP.

Principle and methodology

To illustrate the operating modes of the designed meta-neurons within the TDP, the electric field distributions of the gold -VO_2 hybrid resonators under 0.5 THz incidence at two distinct ambient temperatures are presented in Fig. 2a. Before

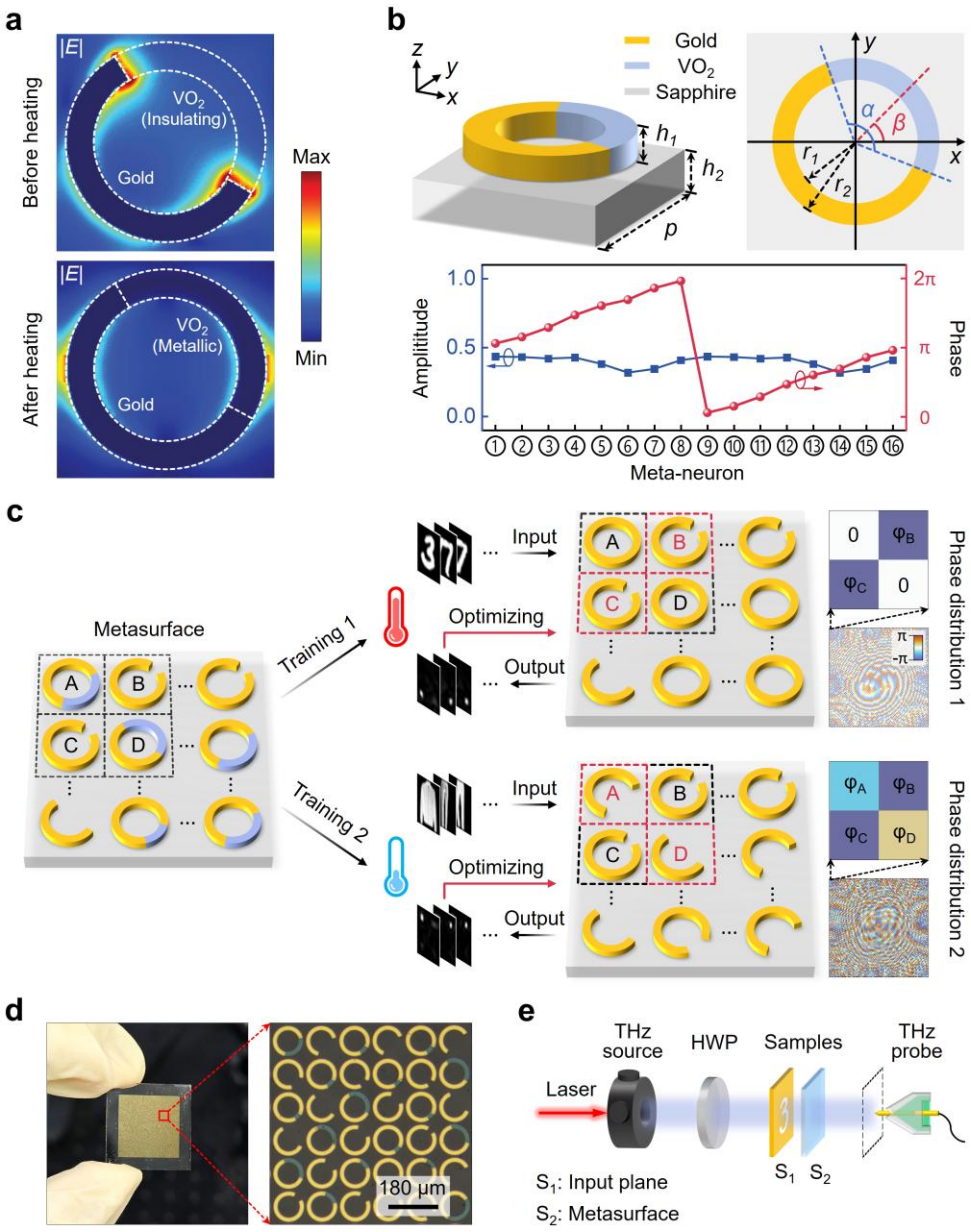


Fig.2 Design principle and experimental setup. a Simulated electric field of the gold-VO_2 hybrid resonators under 0.5 THz incidence before and after heating. **b** Schematic of a meta-neuron within the TDP, and the amplitude and phase delay of transmitted cross-polarization waves via 16 constructed meta-neurons. **c** Model training method. **d** Fabricated sample. **e** Schematic of the experimental setup.

heating (at room temperature, ~300 K), VO_2 remains in the insulating phase and is effectively electrically inactive. As a result, the incident THz waves are scarcely influenced by VO_2, and the electromagnetic response of the hybrid resonator is governed solely by the gold structure (i.e., the C-structure reduces to the corresponding G-structure). In contrast, after heating to 341 K, VO_2

undergoes an insulator-to-metal transition and becomes highly conductive. The gold and VO_2 components then jointly form an electrically continuous hybrid resonator, enabling a closed current loop. Consequently, closed-ring electric-field profiles involving both gold and VO_2 are observed, while the localized field enhancement at the open ends of the gold structure is suppressed. Fig. 2b shows the structure of the meta-neuron, which has a period of p = 120 μm, resonator height of h_1 = 0.2 μm, substrate height of h_2 = 500 μm, inner diameter of r_1 = 40 μm, and outer diameter of r_2 = 55 μm. In our design, the gold resonators are oriented at an angle of β = 45° (or β = -45°) relative to the *x*-axis to achieve orthogonal polarization conversion. At the room temperature, we construct 16 different meta-neurons with varying opening angle α and orientation angle β of the gold resonators, as depicted in Fig. 2b. Under heating conditions, the C-structure form a closed ring resonator, and result in consistent amplitude and phase delay.

Figure 2c illustrates the transfer learning-based optimization method for realizing the temperature-dependent classification functionalities of the TDP. In our design, two types of the meta-neurons (i.e., C-structure and G-structure) within the metasurface are arranged in a checkerboard-like interlaced pattern. For clarity, four meta-neurons are marked within the black dashed boxes, and labeled A, B, C, and D, where A and D are C-structure, while B and C are G-structure, as shown on the left side of Fig. 2c. The model training process can be divided into two steps (labeled as Training 1 and Training 2, respectively). First, we perform the Training 1 under heating conditions. The C-structure meta-neurons form closed ring structure (e.g., meta-neurons A and D) and are assigned a fixed phase value of 0, and only the phase parameters of the G-structure meta-neurons can be optimized (e.g., φ_B and φ_C of the meta-neurons B and C). The 5000 handwritten digits 3 and 5000 handwritten digits 7 from the MNIST training dataset are used as the neural network inputs. In 30 iterations, we minimize the mean squared error (MSE) loss between the neural network outputs and ground truths using the Adam stochastic gradient descent algorithm, details about the neural network training are supplied in Supplementary Section 2. After training, the optimized metasurface phase,

where half of the phase values are 0, can be obtained, labeled as Phase distribution 1. Subsequently, we conduct the Training 2 at room temperature. The phase parameters of the C-structure meta-neurons (e.g., φ_A and φ_D of the meta-neurons A and D) are optimizable, whereas the G-structure meta-neurons are fixed with the phase values transferred from the Training 1. After 30 iterations trained on 5000 coats and 5000 trousers from the Fashion-MNIST training dataset, we obtain the Phase distribution 2.

For experimental validation, we fabricate the TDP with a 120 × 120 array of meta-neurons, as showcased in Fig. 2d. The schematic of the optical setup for experimental characterization of the TDP is illustrated in Fig. 2e. By directing a femtosecond laser beam onto a photoconductive antenna (THz source), THz radiation is generated. This radiation is modulated by a half-waveplate (HWP) and the samples, then diffracted onto a detection plane (black dashed box). At the detection plane, a THz probe collects the electric field distribution, which contains the output information of the TDP. More detailed information about the experimental method is provided in Methods.

Experimental demonstration of the TDP for classification task switching. As a proof of concept, Fig.3 demonstrates the TDP for temperature-dependent classification task switching. The output plane features four discrete detection regions, with the top two for fashion products at room temperature and the bottom two for handwritten digits at elevated temperature. Before heating, the TDP works as a fashion product classifier, as shown in Fig. 3a. First, a coat is selected as the input of the TDP under the illumination of *x*-polarization waves at 0.5 THz. The TDP diffracts the *y*-polarization waves on to the output plane, and the simulation and experiment output results illustrate that the electric field intensity is mainly focused at the top left corner in the output plane. We calculate the normalized electric field energy distribution according to the electric field intensity distributed in the four regions for both simulation and experiment. The energy distribution histogram demonstrates the successfully classification of the input coat. A slight difference between the simulation and experiment in the energy distribution is observed due to the experiment/fabrication errors. Then, a trouser is recognized by the TDP with

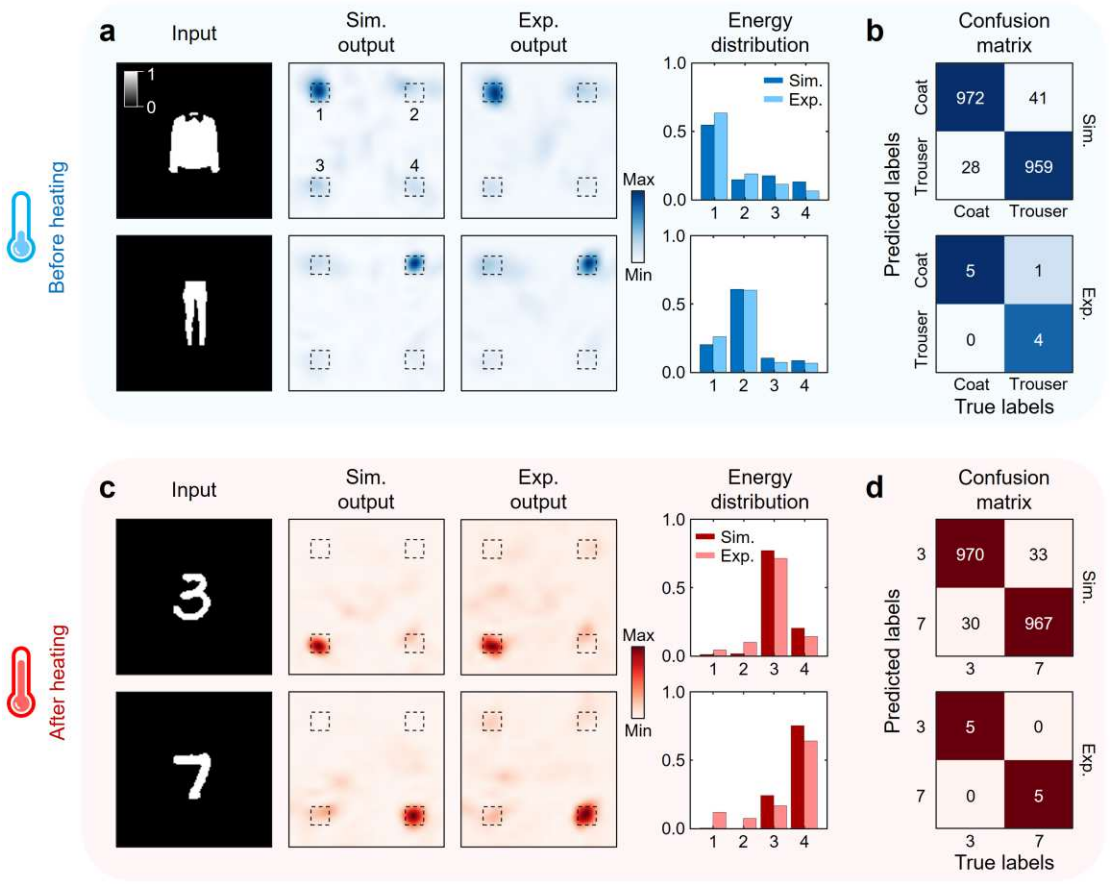


Fig.3 The TDP for thermally controllable classification task switching between fashion products and handwritten digits at 0.5 THz. a, **b** The TDP for the classification of coats and trousers from Fashion-MNIST testing dataset at room temperature, showing simulated and experimental electric field intensity distributions, energy distributions (**a**), and calculated confusion matrices (**b**). **c**, **d** After heating, the TDP classifies handwritten digits 3 and 7 from MNIST testing dataset, with simulated and experimental electric field intensity distributions, energy distributions (**c**), and calculated confusion matrices (**d**).

the electric field intensity is mainly focused on the top right corner in the output plane according to the simulation and experiment output. The calculated normalized energy distribution showcases the accurate classification of the input trouser. To further characterize the classification performance, we calculate the confusion matrix using a total of 2000 coats and trousers in simulation, as well as a total of 10 coats and trousers in experiment, which are from Fashion-MNIST testing dataset (excluded from the training dataset). The classification accuracies are calculated from the confusion matrices that 96.6%

in simulation and 90.0% in experiment. Supplementary Section 3 provides the experimental results of output electric field intensity distributions for five different appearances per category used as the input.

After heating, the TDP switches its functionality into a handwritten digit classifier, and enables the recognition of digits 3 and 7, as illustrated in Fig. 2c. Under the 0.5 THz *x*-polarization waves incidence, the inputs 3 and 7 are processed by the TDP, and then diffracted onto the output plane. The simulation and experiment output of inputs 3 and 7 present that the electric field intensity in the output plane is mainly distributed in the bottom left corner and right corner, respectively. The corresponding energy distributions of simulation and experiment demonstrate the classification capability of TDP for handwritten digits. Figure 2d showcases the calculated confusion matrix leveraging totally 2000 handwritten 3 and 7 in simulation, as well as 10 handwritten 3 and 7 in experiment, which are from the Fashion-MNIST testing dataset excluded from its training dataset. The classification accuracy of 96.9% in simulation and 100% in experiment validate the thermally controllable processing performance of the TDP. Furthermore, we construct a TDP that performs 10-class classification per category (10 fashion products and 10 handwritten digits), which is numerically demonstrated in Supplementary Section 4. In addition, a TDP enables more diverse function switching (e.g., recognition and imaging) is discussed in Supplementary Section 5.

TDP-based double objects classifier.

To further demonstrate the classification performance of the TDP framework, we train and fabricate another TDP to achieve a more complicated task—i.e., the simultaneous classification of double objects. As shown in Fig. 4a, c, four images consisting of trouser/sneaker-trouser/sneaker pairs are selected as neural network inputs at room temperature, and four images of 3/7-3/7 pairs are used as the input at elevated temperature. These images are created by combining two images from Fashion-MNIST and MNIST testing dataset (excluded from their training dataset). In the output plane, eight discrete regions are divided for electric field detection and classification. Regions 1 to 4 are designed for room temperature tasks (region 1: left 3, region 2: right 3, region 3: left 7, region 4: right 7), while regions 5 to 8 are for elevated temperature tasks (region 5: left trouser, region 6: right trouser, region 7: left

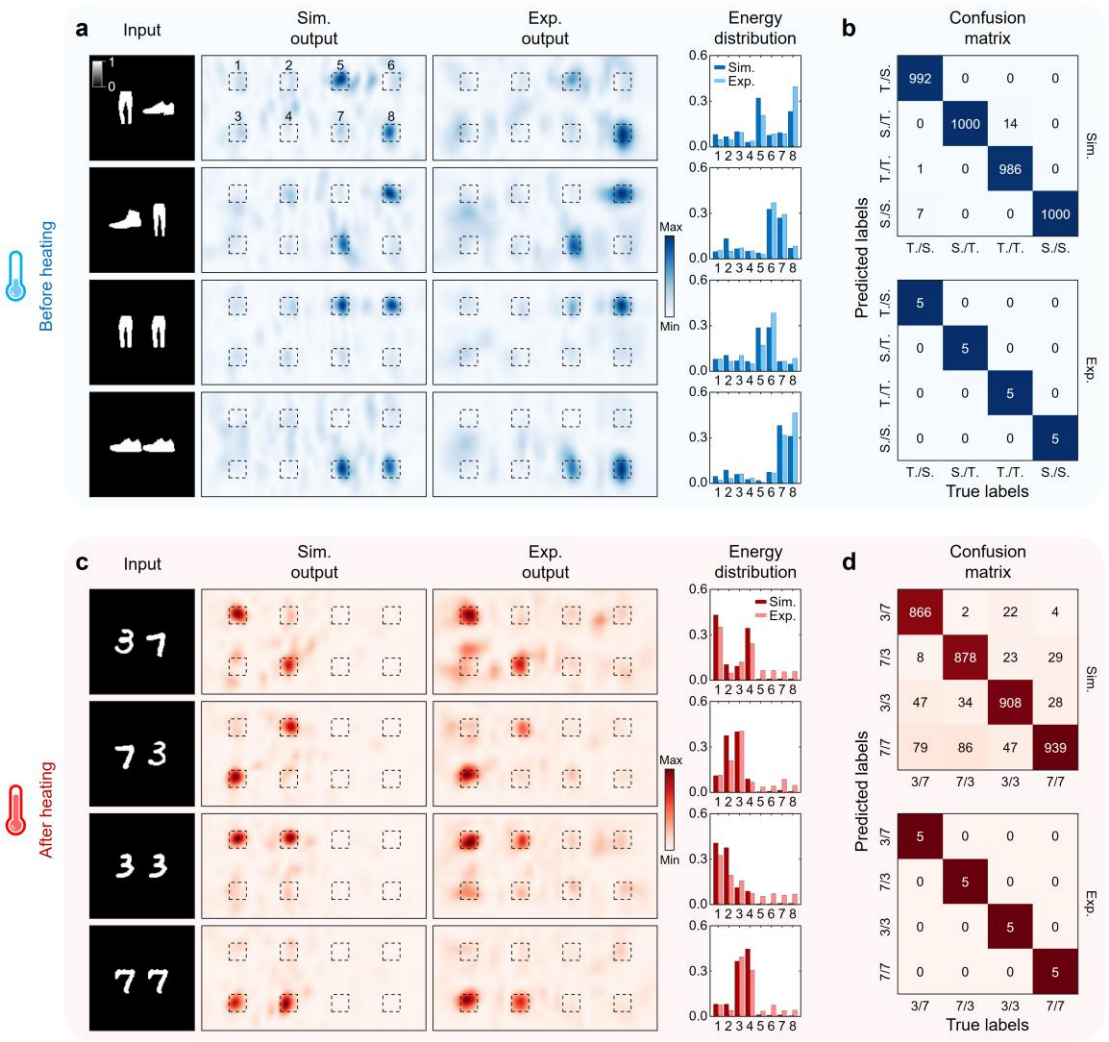


Fig.4 The TDP for recognizing double objects at 0.5 THz incidence. a, **b** For the classification of double fashion products at room temperature, the simulated and experimental electric field intensity distributions, energy distributions (**a**), and calculated confusion matrices (**b**). **c**, **d** After heating, the classification of double handwritten digits, with simulated and experimental electric field intensity distributions, energy distributions (**c**), and calculated confusion matrices (**d**).

sneaker, region 8: right sneaker). At room temperature (Fig. 4a), with the input of four images under the illumination of *x*-polarization waves at 0.5 THz, the simulation and experiment outputs indicate that electric field intensities are mainly distributed in two regions, and the normalized energy distributions demonstrate the successful classification of double fashion products. The calculated confusion matrices present a simulation accuracy of 99.5% and experiment accuracy of 100%, as showcased in Fig. 4b. After heating (Fig. 4c),

four handwritten digit pairs are selected as inputs under the 0.5 THz *x*-polarization waves incidence. In simulation and experiment, the electric field intensity distributions and corresponding energy distributions demonstrate the accurate recognition of double handwritten digits, and the calculated confusion matrices reveal the accuracy of 89.8% and 100%, respectively. The output experimental results for five appearance inputs per category (i.e., 20 different double fashion products and 20 different double handwritten digits) at two distinct temperatures are provided in Supplementary Section 6.

The TDP enable secure information transmission.

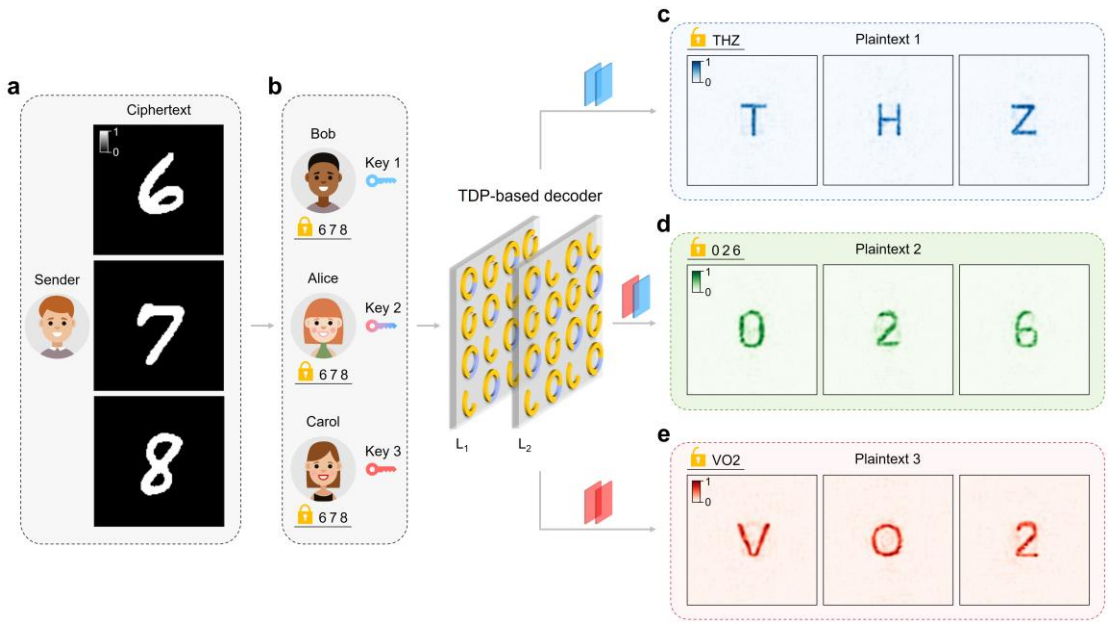


Fig.5 The two-layer TDP for secure information transmission. a Transmitted ciphertext. **b** Three authorized parties hold three distinct decryption keys. **c-e** Decrypted plaintexts obtained using decryption keys (three different temperature conditions) and TDP-based decoder.

One way to protect information is through encryption technology, which converts plaintext into ciphertext for transmission, ensuring that only authorized parties with the correct decryption key can decode the true information. By using ambient temperature as decryption key, the TDP with the capability of intelligent information processing offers a unique method of all-optical encryption to achieve secure information transmission. Figure 5 illustrates the decryption process where the same ciphertext is sent to three different authorized parties, resulting in three distinct decrypted messages by using

three temperature-dependent decryption keys and a two-layer TDP-based decoder. Specifically, as shown in Fig. 5a, a sender transmits ciphertext “678” to authorized parties Bob, Alice, and Carol, respectively. During the transmission, an eavesdropper can only intercept the encrypted message “678”, which are invalid and do not reveal the actual information. Subsequently, Bob, Alice, and Carol use their respective keys (Key1: both layers of the TDP at room temperature, Key2: the first layer of the TDP heated to a specific temperature, Key3: both layers of the TDP heated to a specific temperature) to decode the ciphertext through the TDP-based decoder, as shown in Fig. 5b. This process involves inputting handwritten digits 6, 7, and 8 from MNIST testing dataset into the pre-trained TDP. The training of this TDP is achieved by jointly optimizing networks under different temperature conditions, while using 6, 7, and 8 from MNIST training dataset as inputs and specific plaintext images as ground truths, enabling it to learn the image-to-image mapping. Fig. 5c showcases the output electric field intensity distributions, revealing the plaintext information “THZ” which Bob decrypted using Key 1. Similarly, Alice and Carol decrypt the plaintext information “026” and “VO2” using Key 2 and Key 3, respectively, as presented in Fig 5d, e. To demonstrate robustness, Supplementary Section 7 discusses the output results for the inputs with different appearances.

Conclusion

In summary, by integrating thermally reconfigurable VO_2 resonators with gold resonators, we propose the TDP operating in the THz band that enables temperature-dependent classification function switching. Under two different ambient temperatures, the TDP can switch the function between classifying fashion products and handwritten digits. Furthermore, to verify the parallel processing capability of the TDP, we design and construct another TDP to handle more complex tasks, such as the simultaneous classification of double objects of fashion products and handwritten digits. Finally, we demonstrate that the TDP framework can be extended to achieve data encryption for secure information transmission, where only authorized parties equipped with the temperature-dependent keys can decrypt the transmitted ciphertext. This active all-optical neural network can process distinct tasks under different ambient temperatures, offering a unique method to design intelligent optical systems, and opens new avenues for large scale parallel computing, real-time data

analysis, and optical encryption.

Methods

Training methods

The TDP is trained using the PyTorch framework (version 1.10.2) on a Windows 11 operating system (Microsoft). The hardware includes an Intel(R) Core(TM) i9-13900H central processing unit running at 2.6 GHz, an NVIDIA GeForce RTX 4060 graphics processing unit, and a 16 GB of random-access memory. For optimization of the phase parameters in each layer of the TDP, the mean squared error loss function and the Adam optimizer are employed, with a training batch size of 8 and a learning rate of 0.001.

Experimental setup

We develop a near-field THz time-domain spectroscopy microscopy system to scan the output electric field distribution of the TDP. The system uses a femtosecond laser with a central wavelength of 780 nm, which is split into two paths: one directly drives a photoconductive antenna emitter (THz source) to generate THz waves illuminating the samples, while the other is coupled into a single-mode fiber and delivered to a THz probe tip mounted on a three-axis scanning stage. The samples are fixed on a holder with heating capability, and the THz probe scans behind samples to detect the electric field distribution at the output plane of the TDP.

Device fabrication

A 200-nm-thick VO_2 film was grown on a 500-μm-thick (0001)-oriented sapphire substrate by pulse laser deposition. Before patterning, the sample was cleaned in acetone, ethanol, and deionized water and dried with nitrogen. Then, a photoresist layer (AZ1500) was spin-coated on the sample, and the arc pattern was formed by ultraviolet photolithography. The pattern was transferred into the VO_2 film via reactive ion etching using SF_6, thereby defining the VO_2 structures. Next, the C-shaped ring pattern was defined in a bilayer resist (LOR10B/AZ1500) after the second ultraviolet photolithography. The 10-nm-thick titanium and 200-nm-thick gold films were sputtered by magnetron sputtering, and the metallic structures were formed after the lift-off process in an NMP-based remover. Finally, the sample was rinsed with acetone, ethanol,

and deionized water, followed by nitrogen drying.

Acknowledgements

This work was supported by the National Natural Science Foundation of China (No. 62588201, No. 62271320， No. 62501400 No. 62331015 and No. BK20240062); the National Key Research and Development Program of China (2023YFF0719200 and 2023YFF0717900); and the 111 project (D18014).

Author contributions

Conceptualization: X.Z. Methodology: G.W., X.Z., X.H., and T.Z., Software: G.W., T.Z., and Z.T., Data curation: G.W., X.H., and Z.T. Writing—original draft: G.W., X.Z., X.H., A.P.S., J.W., Y.Z., and S.Z., Visualization: G.W., X.Z., Z.G., J.S., Project administration: X.Z., J.W., B.J., and Y.Z. Funding acquisition: X.Z., J.W., B.J., and Y.Z.

Data availability

All data needed to evaluate the conclusions in the paper are present in the paper and/or the Supplementary Materials

Conflict of interest

The authors declare no competing interests.

References

1. Krizhevsky, A., Sutskever, I. & Hinton, G. E. ImageNet classification with deep convolutional neural networks. *Commun. ACM* **60**, 84–90 (2017).
2. Gehrig, D. & Scaramuzza, D. Low-latency automotive vision with event cameras. *Nature* **629**, 1034–1040 (2024).
3. Xiang, A. et al. Fair human-centric image dataset for ethical AI benchmarking. *Nature* **648**, 97–108 (2025).
4. Collobert, R. et al. Natural Language Processing (Almost) from Scratch. *J. Mach. Learn. Res.* **12**, 2493–2537 (2011).
5. Guo, D. et al. DeepSeek-R1 incentivizes reasoning in LLMs through reinforcement learning. *Nature* **645**, 633–638 (2025).
6. Chen, Y. -H. et al. Eyeriss: An Energy-Efficient Reconfigurable Accelerator for Deep Convolutional Neural Networks. *IEEE J. Solid-St. Circ.* **52**, 127–

138 (2017).
7. Chen, H. et al. Diffractive deep neural networks: Theories, optimization, and applications. *Appl. Phys. Rev.* 2024, **11**, 021332.
8. Fu, T. Optical neural networks: progress and challenges. *Light Sci. App.* **13**, 263 (2024).
9. Zheng, H. et al. Multichannel meta-imagers for accelerating machine vision. *Nat. Nanotechnol.* **19**, 471–478 (2024).
10. Zhang, Y. et al. Memory-less scattering imaging with ultrafast convolutional optical neural networks. *Sci. Adv.* **10**, eadn2205 (2024).
11. Zhu, H. H. et al. Space-efficient optical computing with an integrated chip diffractive neural network. *Nat. Commun.* **13**, 1044 (2022).
12. Shen, Y. et al. Deep learning with coherent nanophotonic circuits. *Nat. Photonics* **11**, 441–446 (2017).
13. Gao, X. et al. Terahertz spoof plasmonic neural network for diffractive information recognition and processing. *Nat. Commun.* **15**, 6686 (2024).
14. Xue, Z. et al. Fully forward mode training for optical neural networks. *Nature* **632**, 280–286 (2024).
15. Lin, X. et al. All-optical machine learning using diffractive deep neural networks. *Science* **361**, 1004-1008 (2018).
16. Hu, J. et al. Diffractive optical computing in free space. *Nat. Commun.* **15**, 1525 (2024).
17. He, C. et al. Pluggable multitask diffractive neural networks based on cascaded metasurfaces. *Opto-Electron. Adv.* **7**, 230005 (2024).
18. Guo, Z. et al. Polarization-selective unidirectional and bidirectional diffractive neural networks for information security and sharing. *Nat. Commun.* **16**, 4492 (2025).
19. Li, X. et al. Simultaneously sorting of arbitrary vector structured beams with spin-multiplexed diffractive metasurfaces. *Adv. Photon. Nexus* **3**, 036010 (2024).
20. Wang, G. et al. Modular Diffractive Neural Networks Using Cascaded Metasurfaces. *Laser Photonics Rev.* **19**, e00923 (2025).
21. Li, J. et al. All-optical complex field imaging using diffractive processors. *Light Sci. App.* **13**, 120 (2024).
22. Li, J. et al. Unidirectional imaging using deep learning–designed materials. *Sci. Adv.* **9**, eadg1505 (2023).
23. Wang, G. et al. High-capacity directional information processor using all-

optical multilayered neural networks. *Sci. Adv.* **11**, eadu0904 (2025).
24. Zhang, T. et al. Integrated Polarization, Distance, and Rotation for Multi-DoF Diffractive Processor and Information Encryption. *Adv. Mater.* **37**, 2506222 (2025).
25. Qian, C. et al. Dynamic recognition and mirage using neuro-metamaterials. *Nat. Commun.* **13**, 2694 (2022).
26. Chen, S. et al. Optical generative models. *Nature* **644**, 903–911 (2025).
27. Liu, C. et al. A programmable diffractive deep neural network based on a digital-coding metasurface array. *Nat. Electron.* **5**, 113–122 (2022).
28. Ning, Y. M. et al. Mechanically Programmable Diffractive Neural Networks Based on Pancharatnam-Berry Phase. *Adv. Funct. Mater.* e12689 (2025).
29. Yu, H. et al. All-optical image transportation through a multimode fibre using a miniaturized diffractive neural network on the distal facet. *Nat. Photon.* **19**, 486–493 (2025).
30. Luo, X. et al. Metasurface-enabled on-chip multiplexed diffractive neural networks in the visible. *Light Sci. Appl.* **11**, 158 (2022).
31. Wang, K. et al. Ultracompact 3D integrated photonic chip for high-fidelity high-dimensional quantum gates. *Sci. Adv.* **11**, eadv5718 (2025).
32. Yu, N. et al. Light Propagation with Phase Discontinuities: Generalized Laws of Reflection and Refraction. *Science* **334**, 333-337 (2011).
33. Dong, B. et al. Switchable Pancharatnam–Berry Phases in Heterogeneously Integrated THz Metasurfaces. *Adv. Mater.* **37**, 2417183 (2025).
34. Li, L. et al. Metalens-array-based high-dimensional and multiphoton quantum source. *Science* **368**, 1487–1490 (2020).
35. Wang, Z. et al. Single-layer spatial analog meta-processor for imaging processing. *Nat. Commun.* **13**, 2188 (2022).
36. Zhang, J. C. et al. Electromagnetic Wave Tailoring: From One Dimension to Multiple Dimensions. *Electromagnetic Science*, **1**, 0030131 (2023).
37. Zhu, Q. et al. Scalable, ultrathin, highly selective and emissive films by microsphere-polymer coupled metasurfaces for passive radiative cooling. *PhotoniX* **6**, 39 (2025).
38. Zhu, Y. et al. Metasurfaces designed by a bidirectional deep neural network and iterative algorithm for generating quantitative field distributions. *Light Adv. Manufact.* **4**, 104–114 (2023).

Supplementary Files

This is a list of supplementary files associated with this preprint. Click to download.

- Supplementary20260207.docx